Hypercrosslinked Polymer Gels as a Synthetic Hybridization Platform for Designing Versatile Molecular Separators

Yan Su, Zaoming Wang, Alexandre Legrand, Takuma Aoyama, Nattapol Ma, Weitao Wang, Ken-Ichi Otake, Kenji Urayama, Satoshi Horike, Susumu Kitagawa, et al.

Hypercrosslinked Polymer Gels as a Synthetic Hybridization Platform for Designing Versatile Molecular Separators

Yan Su,[†,#] Zaoming Wang,[‡,¶,#] Alexandre Legrand,[‡,#] Takuma Aoyama,[§] Nattapol Ma,[¶] Weitao Wang,[†] Ken-ichi Otake,[‡] Kenji Urayama,[§] Satoshi Horike,[‡,¶] Susumu Kitagawa,[*,‡] Shuhei Furukawa,[*,‡,¶] and Cheng Gu[*,†,∥]

[†]State Key Laboratory of Luminescent Materials and Devices, Institute of Polymer Optoelectronic Materials and Devices, South China University of Technology, No. 381 Wushan Road, Tianhe District, Guangzhou 510640, P. R. China

[‡]Institute for Integrated Cell-Material Sciences, Kyoto University, Yoshida, Sakyo-ku, Kyoto 606-8501, Japan

[§]Department of Macromolecular Science and Engineering, Kyoto Institute of Technology, Matsugasaki, Sakyo-ku, Kyoto 606-8585, Japan

[¶]Department of Synthetic Chemistry and Biological Chemistry, Graduate School of Engineering, Kyoto University, Katsura, Nishikyo-ku, Kyoto 615-8510, Japan

[∥]Guangdong Provincial Key Laboratory of Luminescence from Molecular Aggregates, South China University of Technology, No. 381 Wushan Road, Tianhe District, Guangzhou, 510640, P. R. China

KEYWORDS: hypercrosslinked polymers, gels, hybridization, molecular separation

ABSTRACT: Hypercrosslinked polymers (HCPs), amorphous microporous three-dimensional networks based on covalent linkage of organic building blocks are a promising class of materials due to their high surface area and easy functionalization; however, this type of materials lacks processability due to their network rigidity based on covalent crosslinking. Indeed, the development of strategies to improve their solution processability for broader applications remains challenging. Although HCPs have similar three-dimensionally crosslinked networks to polymer gels, HCPs usually do not form gels but insoluble powders. Herein, we report the synthesis of HCP gels from a thermally induced polymerization of a tetrahedral monomer, which undergoes consecutive solubilization, covalent bond formation, colloidal formation, followed by their aggregation and percolation to yield a hierarchically porous network. The resulting gels feature concentration-dependent hierarchical porosities and mechanical stiffness. Furthermore, these HCP gels can be used as a platform to achieve molecular-level hybridization with a two-dimensional polymer during the HCP gel formation. This method provides functional gels and corresponding aerogels with the enhancement of porosities and mechanical stiffness. Used in column- and membrane-based molecular separation systems, the hybrid gels exhibited separation of water contaminants with the efficiency of 97.9% and 98.6% for methylene blue and $KMnO_4$, respectively. This result demonstrated the potentials of the HCP gels and their hybrid derivatives in separation systems requiring macroscopic scaffolds with hierarchical porosity.

Introduction.

Porous organic polymers (POPs) are an emerging class of micro- and meso-porous materials obtained from the covalent linkage of organic building blocks via irreversible coupling reactions.[1] Due to their high porosity, chemical stability, lightweight, tunable porous structures, and tailorable functions, POPs have received significant interests in a wide range of applications in separation,[1] catalysis,[2] sensing,[3] optoelectronics,[4] environmental remediation,[5] and renewable energy.[6] Among amorphous POPs, hypercrosslinked polymers (HCPs), which are obtained from Friedel-Crafts alkylation or self-condensation polymerization of simple organic molecules, stand out by presenting the advantage of mild reaction conditions and inexpensive reagents, compared to other porous organic materials.[4] However, the typical products of HCP synthesis are insoluble powders, limiting their processability into macroscale objects, and thus impeding their practical use. To overcome this issue, several methodologies have recently been developed for shaping HCPs into macroscopic porous objects such as monoliths,[7] thin-films,[8,9] and membranes.[10,11] Foams and aerogels are particularly interesting structures because they allow for the combination of pores at different length scales to facilitate mass transport and enhance the accessibility of the adsorbed molecules to the intrinsic micro- and meso-pores of the HCPs; however, there are only reports of POP gels based on conjugated microporous polymer or imine porous polymer.[12−15] In addition, almost no mechanism study on the formation of POP-based gels was fully performed, making it difficult to further control the gel formation. Moreover, the understanding of the gelation process gives a new opportunity to fabricate hybrid materials with other types of polymer materials, in which both polymer networks are entangled at the molecular level. Indeed, hybridization of HCP (aero)gels with other organic porous materials, such as covalent organic frameworks (COFs),[16,17] is particularly interesting, because it allows not only to combine two porous materials with individual functionalities but also to create hierarchical porosity for the design of versatile hybrid systems offering optimum separation and mass transportation.

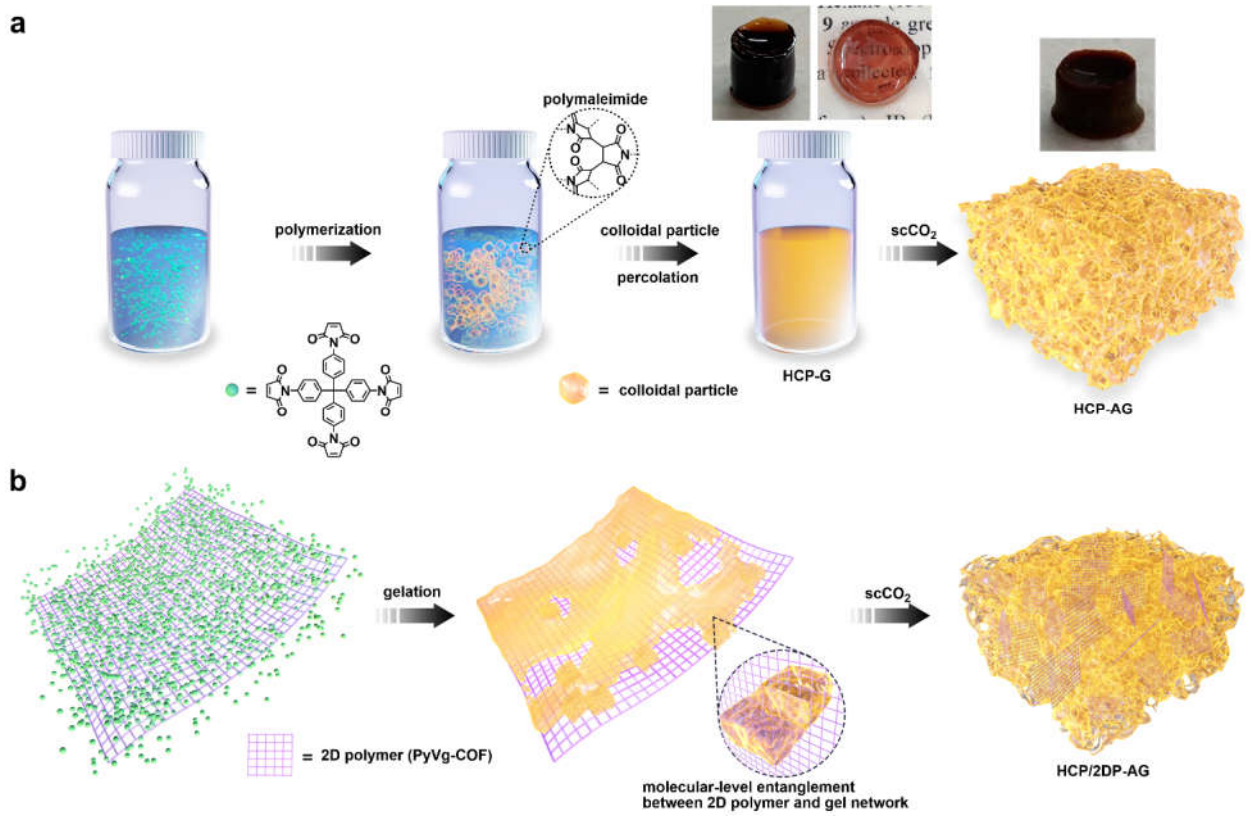

Figure 1. Schematic diagrams for the synthesis of HCP gels and aerogels, and the hybridization of HCP gels with 2D polymers. (a) Synthesis of HCP gels and aerogels via gelation processes, comprising: i) dispersion solution of the monomer in DMF, ii) formation of the colloidal particles, iii) aggregation and percolation of the colloidal particles to form the HCP gel, and iv) solvent exchange with acetone and $scCO_2$ drying to yield the HCP aerogel. The insets are photos of the HCP gel and aerogel. (b) Hybridization with 2D polymer, comprising: i) dispersion solution of the monomer and the 2D polymer in DMF; ii) gelation process inducing the molecular-level entanglement between 2D polymer and gel network; and iii) solvent exchange with acetone and $scCO_2$ drying to yield the hybrid aerogel.

In contrast to the majority of HCP syntheses, which require initiator and/or metal catalyst that inevitably ends up being trapped in the HCPs and eventually influences their porosity, here we report the efficient polymerization of a single-component monomer solution into HCP gel in near-unity yield without the addition of any initiator or catalyst. Indeed, the thermally induced polymerization of a tetrahedral monomer bearing four maleimide groups led to the formation of colloidal particles followed by their aggregation and percolation into an elastic colloidal gel. Insights on the mechanism of the polymerization and the final architecture of the gel were obtained from the combined infrared spectra and dynamic light scattering (DLS) analysis of the monomer solution over the course of the reaction and from the scanning electron microscopy (SEM) images of the corresponding aerogel obtained after solvent removal using supercritical CO_2 ($scCO_2$) drying technique. The resultant aerogels possess combined advantages of hierarchical micropores and mesopores with large surface area, mechanical robustness, and low density. Importantly, such HCP gel can serve as a matrix/substrate for a large variety of materials during the synthetic gelation process, thus providing a platform for designing hybrid soft materials at molecular level. We demonstrate this concept by mixing the monomer solution with a soluble two-dimensional (2D) polymer, which lead to the formation of the HCP gel with enhanced performance in terms of mechanical stiffness and porosity. We highlight the utility of HCP gel-based hybrid materials by developing column- and membrane-based molecular separation systems for purifying water from contaminants.

Results and Discussion.

Synthesis and mechanism study.

We employed a tetrahedral monomer, 1,1',1",1"'-(methanetetrayltetrakis(benzene-4,1-diyl))tetrakis(1H-pyrrole-2,5-dione) (**TPM-4MI**), composed of tetraphenylmethane central core with four maleimide pendant groups linked in a T_d geometry (SI, figures S1–S3), which upon polymerization reaction triggered by heat guarantees the growth of the HCP with a 3D network, high porosity, and uniform pore distribution. In a typical experiment, the HCP gel was synthesized by dispersing the monomer in *N*,*N*-dimethylformamide (DMF) at a concentration of 50.0 mM and sonicated for 1 h, followed by heating at 90 °C in a sealed plastic syringe for 1 day. A deep brown, transparent, and self-standing HCP gel (Figure 1a, inset photos), termed **HCP-G**, was obtained after pushing it out from the syringe. **HCP-G** could be synthesized in various monomer concentrations (50.0, 37.5, 25.0, and 12.5 mM), allowing for controllability over the mechanical properties. The conversion of the gel into the corresponding aerogel, after the solvent exchange with acetone and solvent removal under $scCO_2$ drying by venting up 14 MPa to atmospheric pressure, gave rise to a monolithic aerogel (**HCP-AG**) with retained macroscopic shape (Figure 1a, inset photo), demonstrating no collapse of the porous

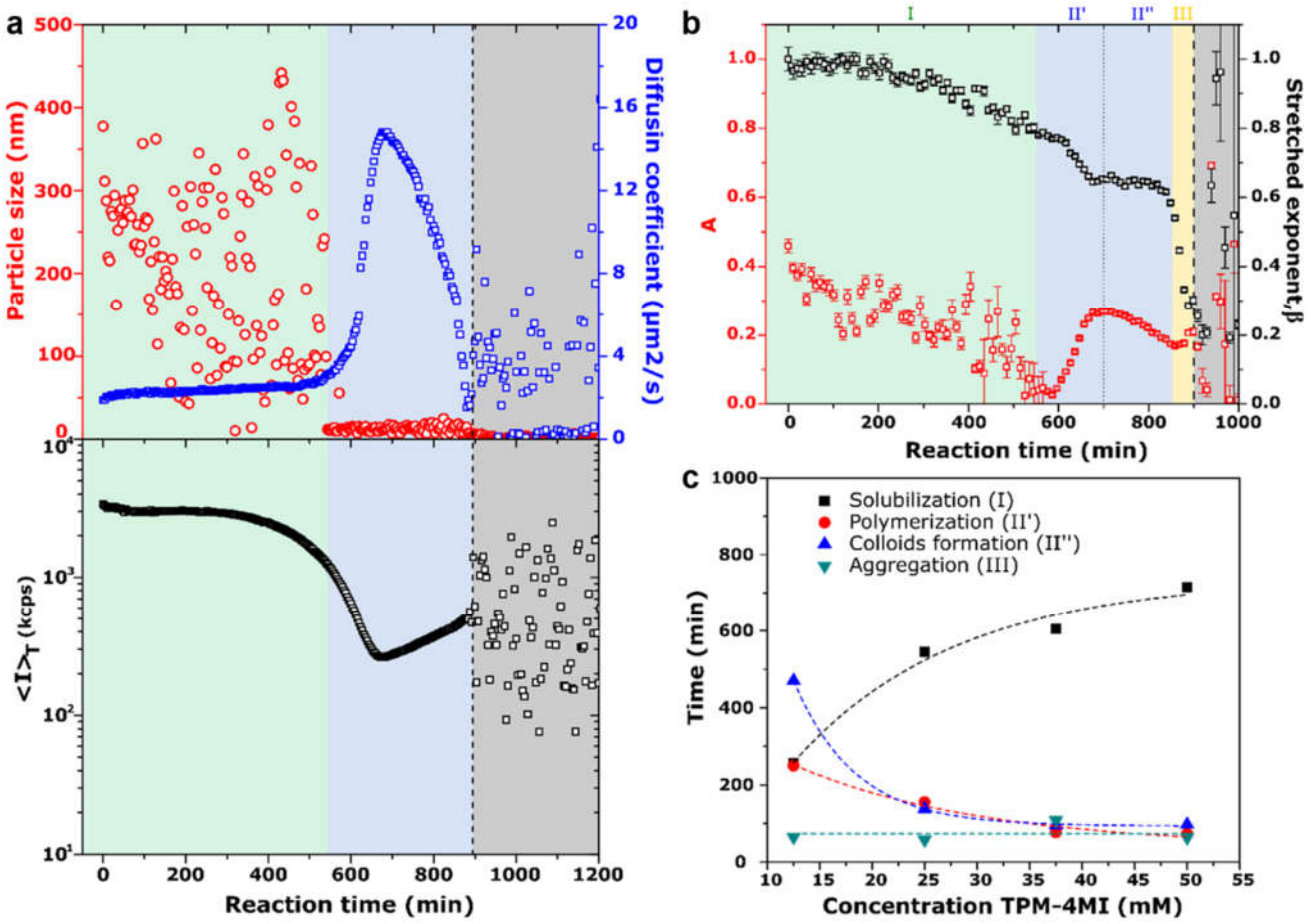

Figure 2. Gel formation of **TPM-4MI** in DMF (25.0 mM) followed by time-resolved dynamic light scattering technique (TR-DLS) at 80 °C. (a) Top: the particle size (red) and diffusion coefficient evolution (blue) and bottom: the time-averaged scattering intensity, $\langle I \rangle_T$, as a function of the reaction time. (b) Variation of the fraction of the fast diffusion mode (A) and stretched exponent (β) as a function of the reaction time. The fraction of the fast diffusion mode (A) and stretched exponent (β) are fitted parameters obtained from the ICFs. (c) Effect of the initial concentration of the **TPM-4MI** solution on the time of the different stages of the reaction leading to the **HCP-G** formation. The different stages of the gel formation are highlighted by green, blue, and orange colored regions corresponding to the solubilization of the organic monomer (I), the polymerization reaction leading to colloidal particle formation (II = II'+II''), and the aggregation of the colloidal particles into a colloidal network (III), respectively. The gelation threshold is represented by the black dashed line. The gray region highlights the effect of the frozen mobility of particles due to gel formation on the DLS response.

structures occurred, which normally would result in a large loss of porosity. Fourier transform infrared (FT-IR) spectra of **HCP-AG** (50.0 mM) revealed a newly generated peak at 1190 cm^{-1} compared to **TPM-4MI**, which can be attributed to the C-C stretching vibration of the polymaleimide, indicating the occurrence of the polymerization reaction (SI, figure S4, table S1). Notably, the peaks at 887 and 643 cm^{-1} in the monomer, attributed to the C-H in-plane bending vibration of cis-olefin, completely disappeared in **HCP-AG**, demonstrating the completeness of the reaction with near-unity yield even at low monomer concentrations (SI, figure S5). In addition, SEM images showed the aerogel to be made of interconnected colloidal particles forming a hierarchical 3D network (Figure 3a, SI, figures S6, S7). Powder X-ray diffraction (PXRD) revealed the amorphous nature of **HCP-AG** (SI, figure S8). The Thermogravimetric (TG) curve showed that **HCP-AG** was thermally stable until 158 °C (SI, figure S9).

In order to investigate the formation of the HCP gel, the polymerization reaction of **TPM-4MI** in DMF, prepared at a concentration of 12.5, 25.0, 37.5, and 50.0 mM, was monitored by time-resolved dynamic light scattering (TR-DLS) measurements at 80 °C. From the *in-situ* monitoring of the scattering elements, insights on (i) the dynamic and kinetic of the polymerization reaction and (ii) the mechanism of gel formation could be obtained. Figure 2a shows the evolution of particle size and diffusion coefficient as a function of the reaction time of a 25.0 mM **TPM-4MI** solution. At the beginning of the heating process, **TPM-4MI** was composed of aggregated molecules as seen from the wide distribution of particle sizes (~200-500 nm) and low diffusion coefficient (stage I, light green area). In the 2nd stage (Stage II) starting at ~550 min, a steep increase of the diffusion coefficient and an abrupt decrease of particle size to a few nm was attributed to the complete solubilization of the monomer molecules and beginning of the polymerization reaction through the covalent linkage of the organic building blocks (blue area). Then, the diffusion coefficient and particle size showed a decrease at ~900 min before becoming null. This was attributed to the infinite colloidal network formation and immobilization of the DMF solvent molecules within the network through capillary forces. Therefore, the general mobility of the

colloidal particles became frozen (dynamical arrest) due to topological constraints rendering reliable measurement by DLS impossible (represented as the gray region). Instead, the evolution of the scattering intensity ($<I>_T$) was a preferred measure to determine the gelation threshold (black dotted line, t_g = 896 min) characterized by the appearance of random fluctuation in $<I>_T$, which was a clear indication of the sol-gel transition. These changes in the particle size and the $<I>_T$ were characteristic of the loss of ergodicity and homogeneity that occurs upon gelation.[18] It is worth noticing that samples prepared at different concentrations present a similar trend, although with different kinetics for stages I and II (SI, figure S10).

TR-DLS measurement and their associated time-averaged intensity correlation function (ICF) could be used to extract additional information on the gelation mechanism. Indeed, the fitting of ICFs in the solution regime by a sum of single and stretched exponentials (see supporting information for more details) could give information on (i) the fraction of the fast diffusion mode (A), which was associated with the mobility of the particle and (ii) the distribution of relaxation times of the slow mode (β), which reflected the uniformity in size of particle formed. Figure 2b shows the evolution of A and β as a function of the reaction time of the 25.0 mM **TPM-4MI** solution. During the solubilization stage (stage I), β and A tended to decrease, which reflected the dispersion of the monomer molecules aggregated into particles of different sizes and with variable mobility. During the 2nd stage (blue area), with continuous heating the A value increased before reaching a plateau, which implied that the fast relaxation mode became the dominant factor. At the same time, β showed a decrease at the beginning of stage II before also reaching a plateau. We attribute this change to the closer proximity of the organic monomer caused by polymerization (stage II'). An indication that the polymerization occurred during stage II' of the reaction was obtained from the quenching of the reaction and isolation of the reactive species from the solution after 1 h sonication, 250, 640, and 760 min of heating at 80 °C. Analysis of the solid samples by FT-IR spectroscopy in attenuated total reflection (ATR) mode showed by the change in the intensity of the characteristic peaks of the C=C and C−H alkene vibration at 1580 cm^{-1} and 1275 cm^{-1}, respectively (SI, figure S13). This was attributed to the polymerization reaction, which only appeared for the sample quenched after 640 min and thus starts during stage II' of the *in-situ* DLS analysis. At t = 700 min, A began to decrease as a slow diffusion mode started to contribute due to the loss of mobility of the polymer chain as they behaved as local oscillators (stage II''). We propose that this reflected the formation of colloidal particles of uniform size (β remains unchanged) and hence similar relaxation times. Indeed, during this reaction time, the growth of colloidal particles reached an average size of 16.0 ± 4.6 nm (SI, figures S6, S7). After 838 min, the colloidal particles began to aggregate and form the premise of the gel network that was assembled at the gelation threshold (t_g = 896 min) through a percolation model. This model described the long-range interconnections of clusters when they grew to fill the available volume. Indeed, the colloids randomly aggregated into cluster of various size distribution as shown by the decrease of β (stage III, orange area), while their mobility A slightly increased before gelation. All samples showed a similar trend, although more difficult to observe at higher concentrations due to the shorter kinetics of stages II', II'', and III (SI, figure S11). A schematic of the gel formation mechanism is proposed in figure S12. From these data, the time for the **TPM-4MI** to (i) polymerize, (ii) form colloidal particle, and (iii) for the latter to aggregate and percolate into a colloidal gel network could be extracted. A concentration dependence of these parameters could be observed (Figure 2c), where increasing the concentration of the **TPM-4MI** led to an increase of solubilization time, a decrease in the polymerization and colloidal formation time, while the time for the colloids to aggregate and percolate remained almost constant.

Mechanical property and porosity.

We assessed the mechanical properties of **HCP-G** and **HCP-AG** by dynamic mechanical analysis (DMA). **HCP-G** (50.0 mM) exhibited apparent flexibility, which could completely spring back without fracture when manually compressed to ~20% volume reduction (Figure 3b). Rheological measurements on **HCP-G** samples showed a concentration-dependence of the mechanical stiffness, where the storage Young's modulus (E') was substantially enhanced from 0.8 to 6.8 kPa by increasing the monomer concentration (12.5 to 37.5 mM), whereas at the highest concentration (50.0 mM) the storage modulus slightly decreased (4.8 kPa). In addition, the gels exhibited frequency-independent storage Young's modulus one order of magnitude higher than the loss Young's modulus (E''), which is characteristic of gel-like behavior (Figure 3c). The value is similar to the one found for metal-organic polyhedra-based[19] and coordination polymer-based[20,21] colloidal gel network, while the mechanical stiffness observed is similar to other soft materials such as gelatine,[22] agarose,[23] and polyvinyl alcohol gels[24] (0.5-70 kPa). Notably, the storage modulus of 6.8 kPa was a fairly high value in all of the organic and organic/inorganic hybrid wet gels,[25–33] thus demonstrating the mechanical robustness of **HCP-G**. On the other hand, the aerogel, **HCP-AG** (50.0 mM), exhibited an enhanced stiffness with E' of 4.9 MPa (SI, figure S14), which was three orders of magnitude higher than those of **HCP-G** and was the top value in the organic and organic/inorganic hybrid aerogels with microporosity.[34–40]

We further evaluated the porosity of **HCP-AG** (50.0 mM) by N_2-sorption measurements at 77 K. The sample exhibited a type I isotherm with the first uptake at a low pressure of $P/P_0 < 0.02$ and slight increment at a medium pressure of $0.02 < P/P_0 < 0.8$ (Figure 3d, SI, figure S15), revealing the micro- and meso-porosity of **HCP-AG**. Notably, at a high pressure of $0.8 < P/P_0 < 1$, **HCP-AG** exhibited a steep increase of the uptake capacity, which corresponded to the condensation of N_2 on the meso- and macro-pores of the aerogel surface by capillarity effect, thus demonstrating the existence of macropores in **HCP-AG**. The Brunauer–Emmett–Teller (BET) surface area of **HCP-AG** (50.0 mM) was calculated to be 1155 m^2 g^{-1} (SI, figure S16), whereas the pore-size distribution profile indicated the dominant micropores at 1 nm combined with mesopores from 3 to 50 nm (Figure 3e, SI, figure S17), demonstrating the hierarchically porous structure of **HCP-AG**. The N_2 sorption profiles, the BET surface areas, and the pore-size distributions of the aerogels prepared from different monomer concentrations were also investigated (Figures 3d, 3e, SI, figures S15–S17). When the monomer concentration was as low as 12.5 mM, the resulting aerogel showed a lower N_2 uptake without presenting capillary condensation at the higher pressure range. This

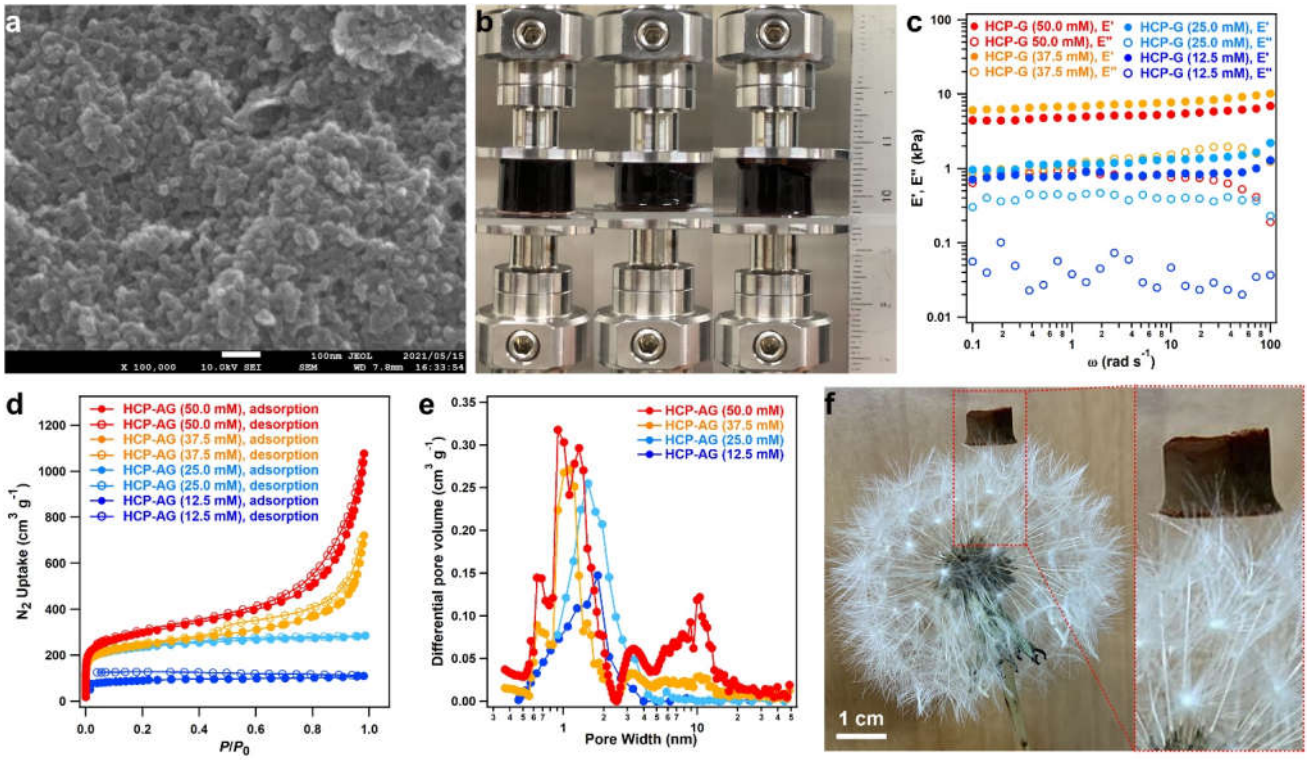

Figure 3. (a) SEM image of **HCP-AG** (50.0 mM). (b) Photos of compressing **HCP-G** (50.0 mM) to ~20% volume reduction and the recovery without fracture. (c) Storage Young's modulus (E′) (filled circles) and loss Young's modulus (E") (hollow circles) of **HCP-G** with different monomer concentrations versus scanning frequency. (d) N_2-sorption isotherms at 77 K for **HCP-AG** with different monomer concentrations. (e) Pore-size distribution curves for **HCP-AG** with different monomer concentrations. (f) Photo of a chunk of 35-mg **HCP-AG** (50.0 mM) resting on top of dandelion hairs.

indicates that the aerogel does not possess meso- and macroporosity, which is also supported by the pore-size distribution curve. When the monomer concentration was increased to 25.0 mM, the microporosity was comparable with those synthesized at higher concentrations, while the macropores only start to appear at a concentration of 37.5 mM (SI, figure S17). These results demonstrated a concentration dependence on the formation of hierarchical porosity explained by the increased number of particles at higher concentrations. Considering the similar volume of the solution, particle size, and time for aggregation for all gel samples, only a more interconnected colloidal network (with the increased number of paths toward percolation) can explain the porosity change; the existence of more colloidal particles increased their possibility to interconnect with each other to form a more crosslinked gel network, which can be supported by the increased mechanical properties at high monomer concentration as discussed above. This highly interconnected gel network resulted in the creation of more mesopores between the colloid particles, contributing to more N_2 sorption at the high-pressure area through capillary condensation. **HCP-AG** was also tested with different gases. For instance, **HCP-AG** (50.0 mM) adsorbed a large amount of CO_2 with capacities of 433 and 51 $cm^3\ g^{-1}$ at 195 and 298 K, respectively (SI, figure S18). This corresponds to an isosteric heat of adsorption (Q_{st}) of 32.0 kJ mol^{-1} (SI, figure S19), which was in sharp contrast to that of N_2 adsorption (12.7 kJ mol^{-1}) and indicated the potentials for their separation.

We found that **HCP-AG** showed a low density of ca. 0.051 g cm^{-3}. In fact, it was so light that a small chunk (ca. 35 mg) can rest comfortably atop the hairs of a dandelion (Figure 3f). Considering the low density and high porosity, **HCP-G** and **HCP-AG** exhibited good mechanical properties with high stiffness for molecular separations (*vide infra*) as water samples can pass through the gel-based columns or membranes without destroying them.

Hybridization with 2D porous polymers.

We chose **PyVg-COF** reported previously by our group as the 2D polymer,[41] which possesses a cationic framework and could self-exfoliate in DMF to yield a homogeneous and transparent solution consisting of well-dispersed 2D monolayers or multilayers without any sedimentation over 6 months. These unique features make **PyVg-COF** very promising for hybridization into a homogeneous and molecular-level manner. The penetration of **TPM-4MI** molecules within the 3.2-nm-sized pores of the **PyVg-COF** monolayer is expected to lead to its hybridization via a molecular-level entanglement when **TPM-4MI** polymerized into a colloidal gel network (Figure 1b). In a typical experiment, **TPM-4MI** (50.0 mM) was serially dispersed in a concentrated **PyVg-COF** solution (1 or 10 mg mL^{-1}), sonicated for 1 h, and heated at 90 °C in a sealed plastic syringe for 1 day to form a deep brown and transparent hybrid gel (termed **HCP/2DP-G**). Then, the solvent of **HCP/2DP-G** was exchanged with acetone and dried with $scCO_2$ to produce the

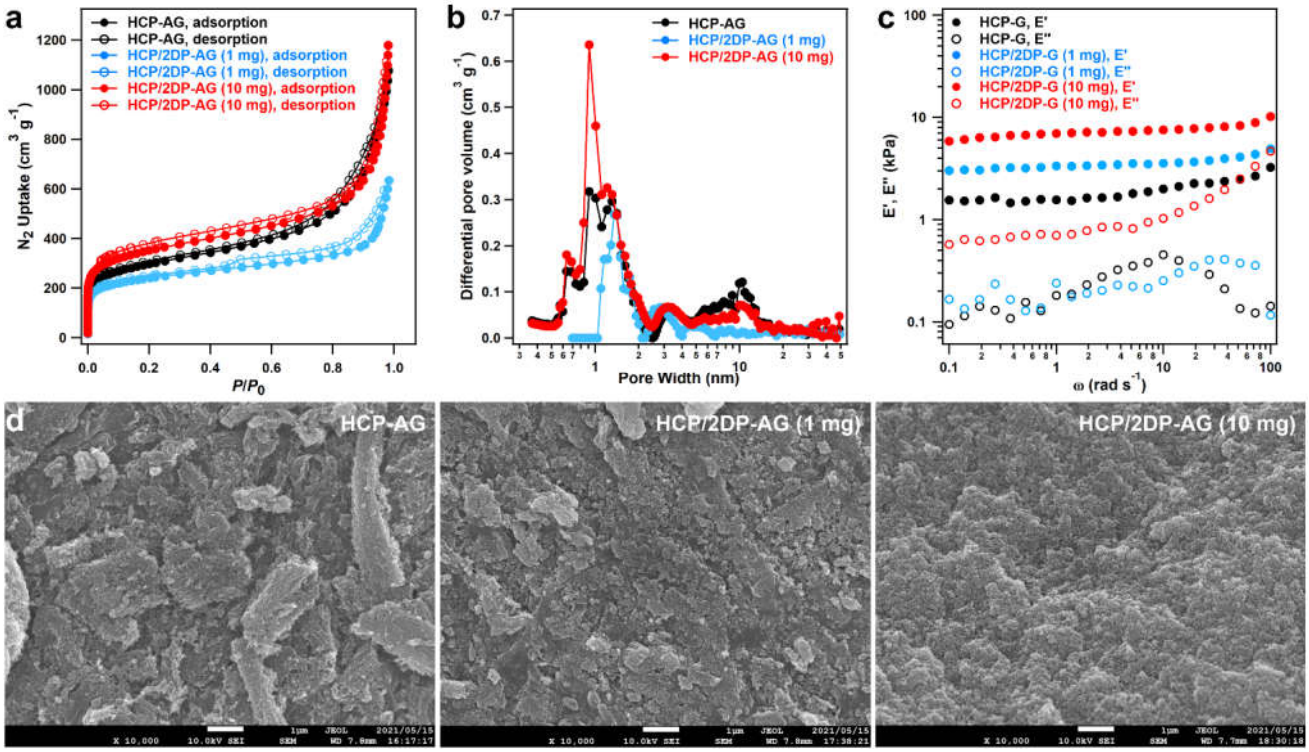

Figure 4. (a) N_2-sorption isotherms at 77 K for **HCP-AG** and **HCP/2DP-AG** (1 mg and 10 mg). (b) Pore-size distribution curves for **HCP-AG** and **HCP/2DP-AG** (1 mg and 10 mg). (c) Storage Young's modulus (E') (filled circles) and loss Young's modulus (E'') (hollow circles) of **HCP-G** and **HCP/2DP-G** (1 mg and 10 mg) versus scanning frequency. (d) SEM images of **HCP-AG** and **HCP/2DP-AG** (1 mg and 10 mg).

corresponding aerogel (**HCP/2DP-AG**) with retained shape. FT-IR spectra revealed the presence of the COF nanosheets did not impede with the polymerization reaction and the gel formation (SI, figure S20). Energy-dispersive X-ray spectroscopy (EDX) measurements revealed the spatial homogeneity of the COF layers in **HCP/2DP-AG** (SI, figure S21). The investigation of the gelation process by TR-DLS of a 25.0 mM **TPM-4MI** solution and **PyVg-COF** revealed that the kinetics of the solubilization of the monomer and the sol-to-gel transition takes similar time to occur in the hybrid system compared to the pristine organic monomer, as indicated by the sudden decrease in particle size after ~ 600 min (vs 550 min) and appearance of the random fluctuation in $\langle I \rangle_T$ at 960 min (vs 896 min), respectively (SI, figure S22). In addition, the presence of the COF 2D sheet renders it difficult to investigate the polymerization reaction and colloidal particles formation when plotting the evolution of A and β as a function of the reaction time (SI, figures S23, S24). However, stage 3 corresponding to the colloidal aggregation, which start after 820 min, is clearly observable with the decrease of β and thus the wider size distribution of the various cluster made of the different number of aggregated colloidal particles (SI, figure S24).

Compared to **HCP-AG**, N_2-sorption experiments for **HCP/2DP-AG** (10 mg) showed increased uptake at low pressure of $P/P_0 < 0.02$ and consistent uptake at high pressure of $0.8 < P/P_0 < 1$, indicating enhanced microporosity and retained macroporosity (Figure 4a, SI, figure S25). The BET surface area of **HCP/2DP-AG** (10 mg) was improved to 1260 $m^2 g^{-1}$ (SI, figure S26). The pore-size distribution profile suggested that the pore volume of **HCP/2DP-AG** (10 mg) was enlarged at the pore size of 1.0 nm compared to **HCP-AG**, whereas it remained equal at the pore size of 50 nm (Figure 4b, SI, figure S27). By contrast, **HCP/2DP-AG** (1 mg) showed a decrease in both the microporosity and mesoporosity, with a BET surface area of 850 $m^2 g^{-1}$ (SI, figures S25–S27), which suggested a concentration-dependent hybridization. When compared to pristine **HCP-AG**, the CO_2 uptakes of **HCP/2DP-AG** (10 mg) were substantially enhanced to 541 $cm^3 g^{-1}$ at 195 K and 63 $cm^3 g^{-1}$ at 298 K (SI, figure S28). The Q_{st} values for CO_2 correspondingly increased from 32 kJ mol^{-1} for **HCP-AG** to 36 kJ mol^{-1} for **HCP/2DP-AG** (10 mg), whereas the Q_{st} values for N_2 decreased from 12.7 kJ mol^{-1} for **HCP-AG** to 9.2 kJ mol^{-1} for **HCP/2DP-AG** (10 mg) (SI, figure S29). These results demonstrated that the hybridization produced synergistic effects on the porosity enhancement, and the cationic 2D polymer promoted the adsorption of polar gases.

As a control experiment, **HCP-AG** was physically blended with **PyVg-COF** in the same weight ratio by grinding. Another control experiment was realized by immersing **HCP-G** in **PyVg-COF** solution in order to attach the latter to the surface of the gel, then followed by the production of the aerogel. In both cases, the microporosity and macroporosity were substantially decreased, resulting in lower BET surface areas of 809 and 706 $m^2 g^{-1}$, respectively (SI, figures S30, S31). These results again showed the synergistic effects of the synthetic hybridization of **HCP/2DP-G**. To further demonstrate the essence of the synergistic effects, we performed ^1H solid-state NMR (ssNMR) for **HCP-AG**, **PyVg-COF**, **HCP/2DP-AG**, and HCP/COF physical blends. The ssNMR revealed a peak shift from 1.59 to 2.08 ppm in **HCP/2DP-AG** compared with **HCP-AG** and HCP/COF physical blends (SI, figure

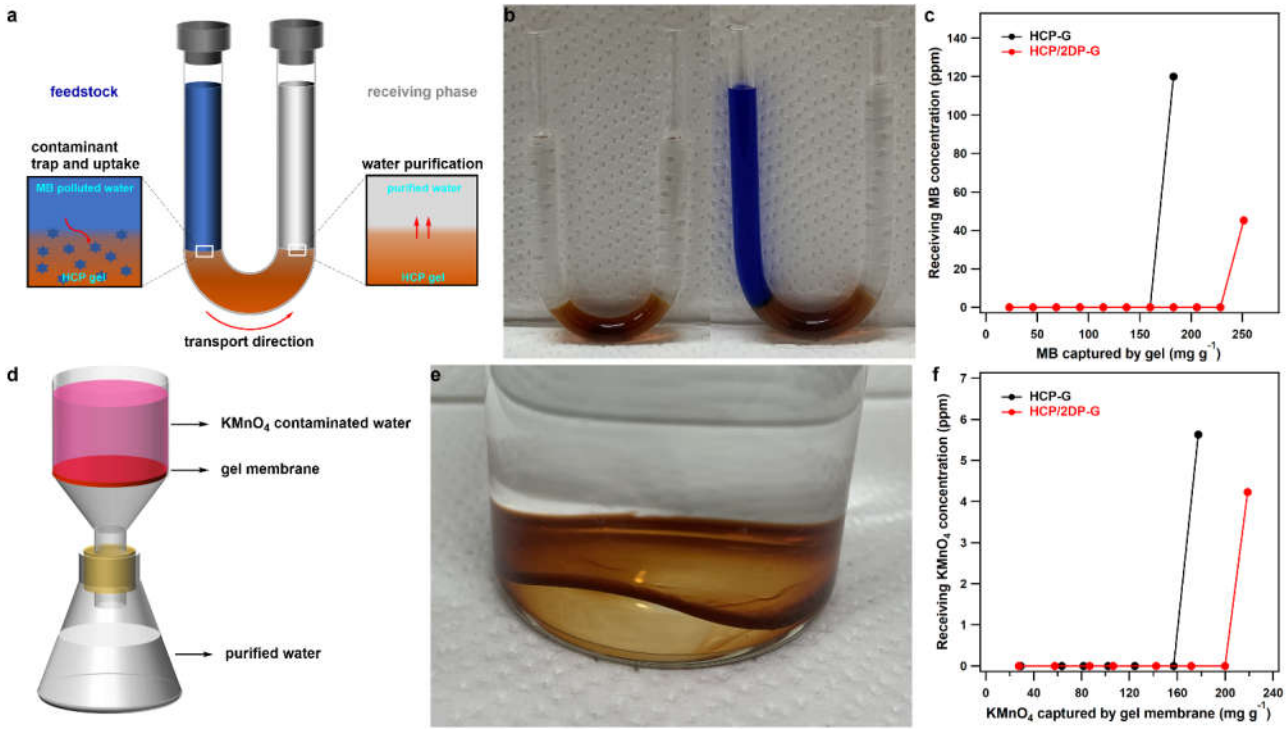

Figure 5. (a) Illustration of the triphasic system setup in the U-shape tube and schematic mechanism of contaminant uptake and water purification processes. (b) Digital photos of the U-shape tube containing the gel at its bottom. Left: the gel after *in situ* synthesis in the tube and solvent exchange with water. Right: The MB-containing water was injected into the feedstock side of the tube and the receiving side started to produce purified water. (c) Breakthrough data for MB uptake using **HCP-G** and **HCP/2DP-G** columns. Receiving MB concentrations are plotted against the amount of MB captured at different time intervals. (d) Illustration of the gel membrane separation system by using simple filtration. (e) Digital photo of the gel membrane. (f) Breakthrough data for $KMnO_4$ uptake using **HCP-G** and **HCP/2DP-G** membranes. Receiving $KMnO_4$ concentrations are plotted against the amount of $KMnO_4$ captured at different time intervals.

S32), indicating that the hybridization was not a simple mixture of the HCP and COF, but a molecular-level entangled network, which works synergistically on the porosity of the hybrid gels.

Actually, the synergistic effects not only affected the porosity but also modified the morphology and mechanical property of the gels. Compared to **HCP-AG** which presented loosely stacked particle connection (SI, figure S6), **HCP/2DP-AG** exhibited much denser and uniform stacking of the particle connection (Figure 4d, SI, figure S33), which suggested enhanced mechanical property. As expected, **HCP/2DP-G** possessed substantially enhanced stiffness, which could be recognized from the simultaneous increment on the storage and loss Young's moduli (Figure 4c). The storage Young's moduli of **HCP/2DP-G** with different 2D polymer concentrations (1 and 10 mg) reached as high as 3.35 and 6.96 kPa, respectively, which were 2.1 and 4.4-folds of that of **HCP-G** (1.57 kPa). On the other hand, the storage Young's modulus of aerogels, **HCP/2DP-AG** (10 mg), reached as high as 7.98 MPa, 1.64-folds of that of **HCP-AG** (SI, figure S34). Additionally, the density of **HCP/2DP-AG** (10 mg) was 0.055 g cm^{-3}, similar to that of **HCP-AG** (0.051 g cm^{-3}). Therefore, **HCP/2DP-G** and **HCP/2DP-AG** possessing synergistically enhanced porosity and mechanical stiffness combined with cationic pore environment are promising to develop molecular separation systems.

Molecular separations.

To highlight the utility of the hybrid gels for molecular separations, we employed versatile separation systems involving column and membrane separations because the HCP gels can be *in situ* synthesized in the shape of the columns and can be readily processed into membranes. First, we employed a gravity-driven U-shape column separation system,[42] in which **HCP-G** and **HCP/2DP-G** were *in situ* synthesized at the bottom of the U-shape columns (Figure 5a). We demonstrate this concept by purifying water from organic dye contaminants. After exchanging the guest DMF solvent with water, such a system could be readily used for the above purpose by adding the feed water from the feedstock side of the column and producing the purified water from the receiving side. We used an organic pollutant methylene blue (MB) as an example to illustrate the purification process. MB aqueous solution was continuously injected into the U-shape column, and the receiving water was subjected to UV-vis spectroscopy measurements to determine the concentration of MB at a certain time interval (Figure 5b). The MB was initially trapped by the gel and gradually passed the column before breaking through it when increasing the amount. This was used to determine the uptake capacity of MB by the gel columns. **HCP/2DP-G** exhibited a substantially higher MB uptake capacity of 229 mg g^{-1} compared to that of **HCP-G** (160 mg g^{-1}) (Figure 5c, SI, figures S35, S36), whereas the separation efficiencies (in terms of the amount of pure water recovered) of **HCP/2DP-G** and **HCP-G** were 97.9% and 94.5%, respectively. The separation performance was benefitted by the enhanced ionic pore environment from the ionic 2D polymer. In principle, such a hybrid system could be utilized in the removal of various contaminants from water, especially those possessing high polarity or ionic species.

Second, we synthesized **HCP-G** and **HCP/2DP-G** on the bottom of large-size glass vials, and after the solvent exchange, they could automatically peel off the glass substrates and form free-standing gel membranes (Figure 5e). We subsequently attached the gel membranes to a funnel and set up a simple membrane-based separation system by filtration (Figure 5d). We used a water sample polluted by a strong oxidant, $KMnO_4$, as an example to illustrate the purification process. $KMnO_4$ aqueous solution was continuously injected onto the membrane, and the receiving water was subjected to UV-vis spectroscopy measurements to determine the concentration of $KMnO_4$ at a certain time interval. $KMnO_4$ was initially blocked and was gradually transported to the bottom of the membrane when increasing its concentration before breaking through the membrane. As expected, **HCP/2DP-G** exhibited a substantially higher $KMnO_4$ uptake capacity of 200 mg g^{-1} compared to that of **HCP-G** (157 mg g^{-1}) (Figure 5f, SI, figures S37, S38), whereas the separation efficiencies of **HCP/2DP-G** and **HCP-G** were 98.6% and 95.3%, respectively. By contrast, the pure **PyVg-COF** membrane was not suitable for the removal of $KMnO_4$ because the membrane slowly dissolved in water, which was confirmed by the UV-vis spectra of the receiving water samples (SI, figure S39). On the other hand, in our hybrid gels, **PyVg-COF** was fixed in the gel networks, whereas its cationic framework provides a strong driving force to the anionic contaminants. Therefore, the synergistic effect of hierarchically porous HCP gel and cationic **PyVg-COF** is essential to construct efficient molecular separators.

The chemical structures of the two gel membranes remained robust after separation, without any oxidation of the network structures, as determined by FT-IR (SI, figure S40). Note that the separation behaviors of $KMnO_4$ and MB are not dependent on the set-up applied because the reversed separations also worked effectively by using the gel-based column for $KMnO_4$ and gel-based membrane for MB (SI, figures S41, S42). Indeed, multi-components separations are observed to be effective by using the gel-based membrane to separate water from both contaminants, as confirmed by the UV-vis spectra of the receiving water (SI, figure S43). The gel-based membranes were reusable with retained separation performance for at least three times (SI, figure 44). The separation performance of anionic contaminants by using our hybrid gels is relatively good even when compared with materials possessing both microporosity and macroporosity from the literature (SI, table S2). Our results demonstrated the capability of processing the pristine and hybridized HCP gels to diverse shapes, which are adaptable for versatile molecular separation platforms.

Conclusion.

In summary, we have successfully synthesized HCP gels from a catalyst-free polymerization of a tetrahedral monomer, yielding the HCP aerogels with synthetically combined micro- and meso-porosity, low density, and high mechanical strength. For the first time, we intensively investigated the gelation process and provided insight into the mechanism. Such HCP gels offered a platform for hybridization with other functional materials such as 2D polymer, which exhibited substantially enhanced porosity and mechanical stiffness. We demonstrated the utility of the hybridized HCP gels by designing column-and membrane-based molecular separation systems, which displayed striking performance on the water-contaminant removal. We expect that our results will facilitate the development of HCPs for separation and other applications requiring porous, macroscopic scaffolds.

ASSOCIATED CONTENT

Supporting Information.
Synthetic procedures, FT-IR, SEM, PXRD, TG, gas adsorption, DMA test, TR-DLS, and UV-vis spectra. This material is available free of charge via the Internet at http://pubs.acs.org.

AUTHOR INFORMATION

Corresponding Author

*gucheng@scut.edu.cn,
shuhei.furukawa@icems.kyoto-u.ac.jp,
kitagawa@icems.kyoto-u.ac.jp

ORCID

Yan Su: 0000-0003-3970-3822
Zaoming Wang: 0000-0003-1385-8164
Alexandre Legrand: 0000-0002-7975-9348
Takuma Aoyama: 0000-0001-6013-8464
Nattapol Ma: 0000-0002-6162-1834
Weitao Wang: 0000-0002-1183-6423
Ken-ichi Otake: 0000-0002-7904-5003
Kenji Urayama: 0000-0002-2823-6344
Satoshi Horike: 0000-0001-8530-6364
Susumu Kitagawa: 0000-0001-6956-9543
Shuhei Furukawa: 0000-0003-3849-8038
Cheng Gu: 0000-0001-5259-6203

Author Contributions

#These authors contributed equally.

Notes

The authors declare no competing financial interest.

ACKNOWLEDGMENT

This work was supported by the National Natural Science Foundation of China (21975078), the Guangdong Basic and Applied Basic Research Foundation (2021A1515010311), the Natural Science Foundation of Guangdong Province (2019B030301003), the 111 Project, and the Thousand Youth Talents Plan. C. Gu, Y. Su, and Z. Wang acknowledge the scholarship support from the China Scholarship Council (Nos. 202006155049, 202006150059, 201806240086). The authors thank the iCeMS Analysis Center for access to analytical instruments.

REFERENCES

(1) Das, S.; Heasman, P.; Ben, T.; Qiu, S. Porous Organic Materials: Strategic Design and Structure–Function Correlation. *Chem. Rev.* **2017**, *117*, 1515.

(2) Zhang, Y.; Riduan, S. N. Functional Porous Organic Polymers for Heterogeneous Catalysis. *Chem. Soc. Rev.* **2012**, *41*, 2083.

(3) Yuan, Y.; Zhu, G. Porous Aromatic Frameworks as a Platform for Multifunctional Applications. *ACS Cent. Sci.* **2019**, *5*, 409.

(4) Tan, L.; Tan, B. Hypercrosslinked Porous Polymer Materials: Design, Synthesis, and Applications. *Chem. Soc. Rev.* **2017**, *46*, 3322.

(5) Alsbaiee, A.; Smith, B. J.; Xiao, L.; Ling, Y.; Helbling, D. E.; Dichtel, W. R. Rapid Removal of Organic Micropollutants from Water by a Porous β-Cyclodextrin Polymer. *Nature* **2016**, *529*, 190.

(6) Kong, D.; Gao, Y.; Xiao, Z.; Xu, X.; Li, X.; Zhi, L. Rational Design of Carbon-Rich Materials for Energy Storage and Conversion. *Adv. Mater.* **2019**, *31*, 1804973.

(7) Yang, X.; Tan, L.; Xia, L.; Woo, C. D.; Tan, B. Hierarchical Porous Polystyrene Monoliths from PolyHIPE. *Macromol. Rapid Commun.* **2015**, *36*, 1553.

(8) Ding, L.; Zhang, A.; Li, W.; Bai, H.; Li, L. Multi-Length Scale Porous Polymer Films from Hypercrosslinked Breath Figure Arrays. *J. Colloid Interface Sci.* **2016**, *461*, 179.

(9) Yang, Y.; Tan, B.; Wood, C. D. Solution-Processable Hypercrosslinked Polymers by Low Cost Strategies: A Promising Platform for Gas Storage and Separation. *J. Mater. Chem. A* **2016**, *4*, 15072.

(10) Qiao, Z.-A.; Chai, S.-H.; Nelson, K.; Bi, Z.; Chen, J.; Mahurin, S. M., Zhu, X.; Dai, S. Polymeric Molecular Sieve Membranes via in situ Cross-Linking of Non-Porous Polymer Membrane Templates. *Nat. Commun.* **2014**, *5*, 3705.

(11) Lau, C. H.; Mulet, X.; Konstas, K.; Doherty, C. M.; Sani, M.-A.; Separovic, F.; Hill, M. R., Wood, C. D. Hypercrosslinked Additives for Ageless Gas-Separation Membranes. *Angew. Chem. Int. Ed.* **2016**, *55*, 1998.

(12) Li, H.; Li, J.; Thomas, A.; Liao, Y. Ultra-High Surface Area Nitrogen-Doped Carbon Aerogels Derived from a Schiff-Base Porous Organic Polymer Aerogel for CO_2 Storage and Supercapacitors. *Adv. Funct. Mater.* **2019**, *29*, 1904785.

(13) Du, R.; Zhang, N.; Xu, H.; Mao, N.; Duan, W.; Wang, J.; Zhao, Q.; Liu, Z.; Zhang, J. CMP Aerogels: Ultrahigh-Surface-Area Carbon-Based Monolithic Materials with Superb Sorption Performance. *Adv. Mater.* **2014**, *26*, 8053.

(14) Zhang, J.; Liu, L.; Liu, H.; Lin, M.; Li, S.; Ouyang, G.; Chen, L.; Su, C.-Y. Highly Porous Aerogels based on Imine Chemistry: Syntheses and Sorption Properties. *J. Mater. Chem. A* **2015**, *3*, 10990.

(15) Zhou, B.; Liu, L.; Yang, Z.; Li, X.; Wen, Z.; Chen, L. Porous Organic Polymer Gel Derived Electrocatalysts for Efficient Oxygen Reduction. *ChemElectroChem* **2019**, *6*, 485.

(16) Haase, F.; Lotsch, B. V. Solving the COF Trilemma: towards Crystalline, Stable and Functional Covalent Organic Frameworks. *Chem. Soc. Rev.* **2020**, *49*, 8469.

(17) Ying, Y.; Tong, M.; Ning, S.; Ravi, S. K.; Peh, S. B.; Tan, S. C.; Pennycook, S. J.; Zhao, D. Ultrathin Two-Dimensional Membranes Assembled by Ionic Covalent Organic Nanosheets with Reduced Apertures for Gas Separation. *J. Am. Chem. Soc.* **2020**, *142*, 4472.

(18) Shibayama, M.; Norisuye, T. Gel Formation Analyses by Dynamic Light Scattering. *Bull. Chem. Soc. Jpn.* **2002**, *75*, 641.

(19) Legrand, A.; Craig, G. A.; Bonneau, M.; Minami, S.; Urayama, K.; Furukawa, S. Understanding the Multiscale Self-Assembly of Metal–Organic Polyhedra towards Functionally Graded Porous Gels. *Chem. Sci.* **2019**, *10*, 10833.

(20) Mukhopadhyay, R. D.; Das, G.; Ajayaghosh, A. Stepwise Control of Host-Guest Interaction Using a Coordination Polymer Gel. *Nat. Commun.* **2018**, *9*, 1987.

(21) Nirmala, A.; Mukkatt, I.; Shankar, S.; Ajayaghosh, A. Thermochromic Color Switching to Temperature Controlled Volatile Memory and Counter Operations with Metal-Organic Complexes and Hybrid Gels. *Angew. Chem. Int. Ed.* **2021**, *60*, 455.

(22) Poveda-Reyes, S.; Moulisova, V.; Sanmartín-Masiá, E.; Quintanilla-Sierra, L.; Salmerón-Sánchez, M.; Ferrer, G. G. Gelatin-Hyaluronic Acid Hydrogels with Tuned Stiffness to Counterbalance Cellular Forces and Promote Cell Differentiation. *Macromol. Biosci.* **2016**, *16*, 1311.

(23) Heidari, H.; Taylor, H. Multilayered Microcasting of Agarose–Collagen Composites for Neurovascular Modeling. *Bioprinting* **2020**, *17*, e00069.

(24) Lyons, J. G.; Geever, L. M.; Nugent, M. J. D.; Kennedy, J. E.; Higginbotham, C. L. Development and Characterisation of an Agar–Polyvinyl Alcohol Blend Hydrogel. *J. Mech. Behav. Biomed. Mater.* **2009**, *2*, 485.

(25) Carné-Sánchez, A.; Craig, G. A.; Larpent, P.; Hirose, T.; Higuchi, M.; Kitagawa, S.; Matsuda, K.; Urayama, K.; Furukawa, S. Self-Assembly of Metal-Organic Polyhedra into Supramolecular Polymers with Intrinsic Microporosity. *Nat. Commun.* **2018**, *9*, 2506.

(26) Jiang, Q.; Zhao, D.; Wang, J.; Yan, H.; Cao, S.; Qiu, Y.; Wang, H.; Liao, Y.; Xie, X. Light Regulation and Long-Lived Stability of RGB Colors in Cholesteric Liquid Crystal Physical Gels via a Mixing Strategy. *Soft Matter* **2021**, *17*, 3216.

(27) Pérez-Calixto, D.; Amat-Shapiro, S.; Zamarrón-Hernández, D.; Vázquez-Victorio, G.; Puech, P.-H.; Hautefeuille, M. Determination by Relaxation Tests of the Mechanical Properties of Soft Polyacrylamide Gels Made for Mechanobiology Studies. *Polymers* **2021**, *13*, 629.

(28) Zhukhovitskiy, A. V.; Zhong, M.; Keeler, E. G.; Michaelis, V. K.; Sun, J. E. P.; Hore, M. J. A.; Pochan, D. J.; Griffin, R. G.; Willard, A. P.; Johnson, J. A. Highly Branched and Loop-Rich Gels via Formation of Metal-Organic Cages Linked by Polymers. *Nat. Chem.* **2016**, *8*, 33.

(29) Vallejo-Sánchez, D.; Amo-Ochoa, P.; Beobide, G.; Castillo, O.; Fröba, M.; Hoffmann, F.; Luque, A.; Ocón, P.; Pérez-Yáñez, S. Chemically Resistant, Shapeable, and Conducting Metal-Organic Gels and Aerogels Built from Dithiooxamidato Ligand. *Adv. Funct. Mater.* **2017**, *27*, 1605448.

(30) Abraham, J. N.; Joseph, S.; Trivedi, R.; Karle, M. Injectable Dextran-fluorenylmethoxycarbonyl Phenylalanine Composite Hydrogels with Improved Mechanical Properties. *Polym. Int.* **2021**, *70*, 222.

(31) Lin, D.; Kelly, A. L.; Maidannyk, V.; Miao, S. Effect of Structuring Emulsion Gels by Whey or Soy Protein Isolate on the Structure, Mechanical Properties, and in-vitro Digestion of Alginate-based Emulsion Gel Beads. *Food Hydrocoll.* **2021**, *110*, 106165.

(32) Hardy, J. G.; Cao, X.-y.; Harrowfield, J.; Lehn, J.-M. Generation of Metallosupramolecular Polymer Gels from Multiply Functionalized Grid-Type Complexes. *New J. Chem.* **2012**, *36*, 668.

(33) Wu, B.; Yang, C.; Xin, Q.; Kong, L.; Eggersdorfer, M.; Ruan, J.; Zhao, P.; Shan, J.; Liu, K.; Chen, D.; Weitz, D. A.; Gao, X. Attractive Pickering Emulsion Gels. *Adv. Mater.* **2021**, *33*, 2102362.

(34) Zhu, D.; Zhu, Y.; Yan, Q.; Barnes, M.; Liu, F.; Yu, P.; Tseng, C.-P.; Tjahjono, N.; Huang, P.-C.; Rahman, M. M.; Egap, E.; Ajayan, P. M.; Verduzco, R. Pure Crystalline Covalent Organic Framework Aerogels. *Chem. Mater.* **2021**, *33*, 4216.

(35) Ma, Y.; Yue, Y.; Zhang, H.; Cheng, F.; Zhao, W.; Rao, J.; Luo, S.; Wang, J.; Jiang, X.; Liu, Z.; Liu, N.; Gao, Y. 3D Synergistical MXene/Reduced Graphene Oxide Aerogel for a Piezoresistive Sensor. *ACS Nano* **2018**, *12*, 3209.

(36) Tang, X.; Zhou, H.; Cai, Z.; Cheng, D.; He, P.; Xie, P.; Zhang, D.; Fan, T. Generalized 3D Printing of Graphene-based Mixed-Dimensional Hybrid Aerogels. *ACS Nano* **2018**, *12*, 3502.

(37) Martín-Illán, J. Á.; Rodríguez-San-Miguel, D.; Castillo, O.; Beobide, G.; Perez-Carvajal, J.; Imaz, I.; Maspoch, D.; Zamora, F. Macroscopic Ultralight Aerogel Monoliths of Imine-based Covalent Organic Frameworks. *Angew. Chem. Int. Ed.* **2021**, *60*, 13969.

(38) Li, F.; Ding, L.-G.; Yao, B.-J.; Huang, N.; Li, J.-T.; Fu, Q.-J.; Dong, Y.-B. Pd Loaded and Covalent-Organic Framework Involved Chitosan Aerogels and Their Application for Continuous Flow-through Aqueous CB Decontamination. *J. Mater. Chem. A* **2018**, *6*, 11140.

(39) Mohammed, A. K.; Usgaonkar, S.; Kanheerampockil, F.; Karak, S.; Halder, A.; Tharkar, M.; Addicoat, M.; Ajithkumar, T. G.; Banerjee, R. Connecting Microscopic Structures, Mesoscale Assemblies, and Macroscopic Architectures in 3D-Printed Hierarchical Porous Covalent Organic Framework Foams. *J. Am. Chem. Soc.* **2020**, *142*, 8252.

(40) Li, C.; Yang, J.; Pachfule, P.; Li, S.; Ye, M.-Y.; Schmidt, J.; Thomas, A. Ultralight Covalent Organic Framework/Graphene Aerogels with Hierarchical Porosity. *Nat. Commun.* **2020**, *11*, 4712.

(41) Wang, L.; Zeng, C.; Xu, H.; Yin, P.; Chen, D.; Deng, J.; Li, M.; Zheng, N.; Gu, C.; Ma, Y. A Highly Soluble, Crystalline Covalent Organic Framework Compatible with Device Implementation. *Chem. Sci.* **2019**, *10*, 1023.

(42) Nguyen, B.-N. T.; Thoburn, J. D.; Grommet, A. B.; Howe, D. J.; Ronson, T. K.; Ryan, H. P.; Bolliger, J. L.; Nitschke, J. R. Coordination Cages Selectively Transport Molecular Cargoes Across Liquid Membranes. *J. Am. Chem. Soc.* **2021**, *143*, 12175.

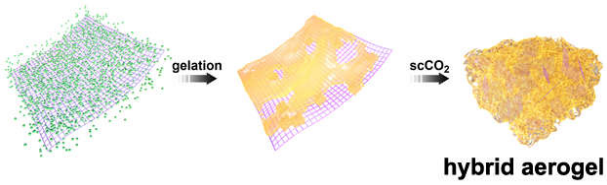
gelation
scCO2
hybrid aerogel